Near field x-ray lithography simulations for printing fine bridges

Antony J Bourdillon[1], **Chris B Boothroyd**[2], **Gwyn P Williams**[3]
and Yuli Vladimirsky[1]

[1] UhrlMasc Inc., PO Box 700001, San Jose, CA 95170-0001, USA
[2] IMRE, 3 Research Link, Singapore 117602
[3] Jefferson National Accelerator Facility, Jefferson Avenue, Newport News, VA 23606, USA

E-mail: bourdillona@prodigy.net

Abstract

By using the near field in proximity x-ray lithography (PXL), a technique is
demonstrated that extends beyond a resolution of 25 nm print feature size for
dense lines. 'Demagnification by bias' of clear mask features is positively
used in Fresnel diffraction together with multiple exposures of sharp peaks.
Exposures are performed without lenses or mirrors between the mask and
wafer, and 'demagnification' is achieved in a selectable range, $1\times$–$9\times$. The
pitch is kept small by multiple stepped exposures of sharp, intense image
peaks followed by single development. Low pitch nested lines are
demonstrated. The optical field is kept compact at the mask. Since the
mask–wafer gap scales as the square of the mask feature size, the mask
feature sizes and mask–wafer gaps are comparatively large. Because the
features are themselves larger, the masks are more easily manufactured.
Meanwhile, exposure times for development levels high on sharp peaks are
short, and there are further benefits including defect reduction, virtual
elimination of sidebands, etc. A critical condition (CC) has been identified
that is typically used for the highest resolution. Many devices, including
batches of microprocessors, have been demonstrated previously by
traditional $1\times$ PXL, which is the only next generation lithography
developed and which is now further extended. For two-dimensional near
field patterning, temporal and spatial incoherence at the CC have been used
to show not only that peculiarities in the aerial pattern, such as 'ripple' and
'bright spots', can be virtually eliminated but also that there is an optimum
demagnification, around $3\times$, in the Fresnel diffraction, where the contrast
and, therefore, critical dimension control are highest. In the simulation of a
bridge pattern, 'ripple' is likewise controlled. Blur and run-out are
compared for various sources. Magnification corrections can be applied by
various means. Extension to 15 nm printed features is predicted.

1. Introduction

Proximity x-ray lithography (PXL) is, on the International
Technology Roadmap for Semiconductors, a contender
for application in next generation lithography. PXL is
extensible to 15 nm print resolution using near field rays and
demagnification by bias, without lenses or mirrors [1, 2]. Prints
with feature size down to 25 nm have been demonstrated
[1–5]. Typical 1–2 kV broadband incident beam energies
(1.2–0.6 nm wavelengths) were used, and demagnifications
down to $6\times$ were obtained. The mask feature sizes and
mask–wafer gaps were large, about $20\,\mu$m. The technique,
which has many novel features and is sometimes called
ultra-high resolution lithography (UHRL) [6, 7], employs
Fresnel diffraction positively near a 'critical condition' (CC)
(see later and [2]) and results in demagnification by bias.
While the print is smaller than the corresponding clear mask
feature, the demagnification is not generally uniform because

the bias is more or less constant around the edge of the image, so that the bias is subtracted from the size of the mask aperture when the print is developed. Meanwhile, the optical field is kept compact as in traditional 1× PXL. Dense nested features are obtained and demonstrated [1] by rapid multiple exposures of sharp peaks and single development. Demagnification has considerable importance in a wide range of applications including integrated circuit manufacture and manufacture of micro electromechanical systems. The importance is due additionally to the relative physical simplicity of proximity methods over competing projection systems, as also to relatively high throughputs and simpler equipment requirements.

Thus PXL, which is the only next generation lithography that has been properly demonstrated [8–11], is extensible beyond previously supposed limits [12, 13]. Typically, synchrotron radiation is used as the radiation source and this is naturally collimated by relativity so that the penumbra is controlled to within 1 nm. To provide uniform illumination, the x-ray beam is typically scanned, off an oscillating, grazing-incidence mirror, across the mask–wafer system. Exposures of full fields, typically 50×30 mm, are made in times less than 1 s. The mask is held stationary while the wafer is stepped and aligned between exposures on different fields. A 300 mm wafer will accommodate about 30 such fields. The field at the mask has the same dimensions, namely 50×30 mm. Other sources have individual characteristics and benefits in particular circumstances.

Previously, we have reported results of simulations [14] that have shown the effects of (a) varying the mask–wafer gap about the CC; (b) the residual effects of small absorber transmission; (c) the distortion to be observed in non-symmetric, two-dimensional features; (d) high frequency 'ripple' and 'bright spots' parallel to longer dimensions; (e) mask shaping to virtually eliminate the 'ripple' and 'bright spots'; (f) combined doses due to multiple exposures used to reduce the pitch : line-width ratio [2, 14]. Simulations have been performed for both monochromatic incident radiation and for the wide band of wavelengths typically used in PXL. The simulations generally correspond to experimental demonstrations [1–5].

The choice of magnification has previously been left open to compromises involving mask feature size, gap width, printed feature size, etc. However, there are indeed preferential regimes determined by Fresnel diffraction. Further theoretical understanding is needed of the effects of temporal and spatial coherence on the aerial images produced by Fresnel diffraction. The analysis can be used to identify demagnification regimes that provide enhanced critical dimension (CD) control. The analysis can be further used to illustrate limitations in traditional 1× PXL and to optimize mask patterns for ideal print shapes.

We have previously listed other attempts at fine printing by methods equivalent to 1× contact printing [2]. There have been further incremental attempts to enhance PXL, some of which can, in principle, be employed in near field to be extended further to 15 nm printed features. Some attempts have been uncompetitive for high resolution [15] and involve unnecessarily complicated procedures in 1× mask making and exposure for phase shifting. More significant is the

attempt to use shorter wavelength x-rays, about 0.4 nm, with diamond-like mask substrates [16, 17] and modified resists. It is clear that such incremental resolution enhancements can be improved by a large factor of 3 when adapted to near field. This is partly due to the larger mask–wafer gaps that can be employed, since the gap scales as the square of clear mask feature size. We review the state of near field and proceed to apply theoretical models for understanding temporal and spatial coherence in PXL. This will affect the optimum demagnification that is conducive to high resolution, high contrast and good CD control. The simulations shown here have particular reference to printing fine bridges.

2. Sweet spot

2.1. Currents or flux distribution from a clear mask feature

The most striking graphic demonstration of the necessity for demagnifying clear mask features when high resolution is needed in PXL comes from simulations of currents transmitted by clear mask features. Further details showing the effects of residual absorber transmission are given elsewhere [2].

Figure 1 is a universal dimensionless aerial image showing the distribution of current or light flux, *in vacuo*, below a clear mask feature. The dimensionless figure applies to any particle or light beam having wave-like properties. If the clear mask feature has a width of 150 nm and the wavelength is 0.8 nm, then the vertical range shown is about 40 μm. With 0.4 nm wavelength, the range is 80 μm. It can be seen that there is a long 'sweet spot' about one quarter down, where the current is bright and narrow. This contains the region near the CC, defined later. Here, by controlled development, the highest resolution can be obtained with excellent contrast since the single peak in the aerial image is very narrow. A further theoretical description of this optimum is given below. Notice that figure 1 illustrates the flow of currents or light flux prior to absorption in the resist.

2.2. Schematic for demagnification by bias with multiple exposures

The peak is illustrated in the schematic figure 2, where the sharp peak at the CC allows rapid exposure above a broad
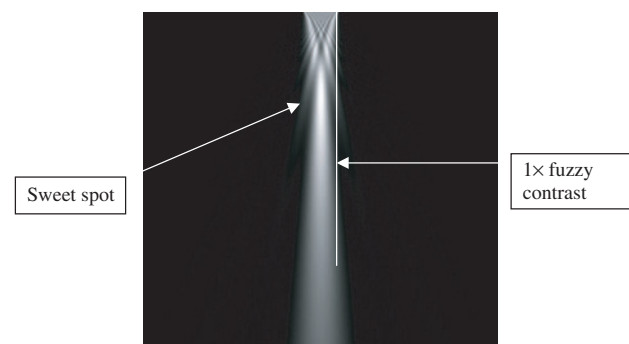

Figure 1. Universal simulation for a Fresnel diffracted current or light flux distribution. If the wavelength $\lambda = 0.8$ nm, passing through a slit of width 150 nm, the picture width is 1536 nm and the height 40 μm. The CC lies at a gap of 10 μm. Note here the sharp peak and adjacent shoulders as in figure 6(*b*).
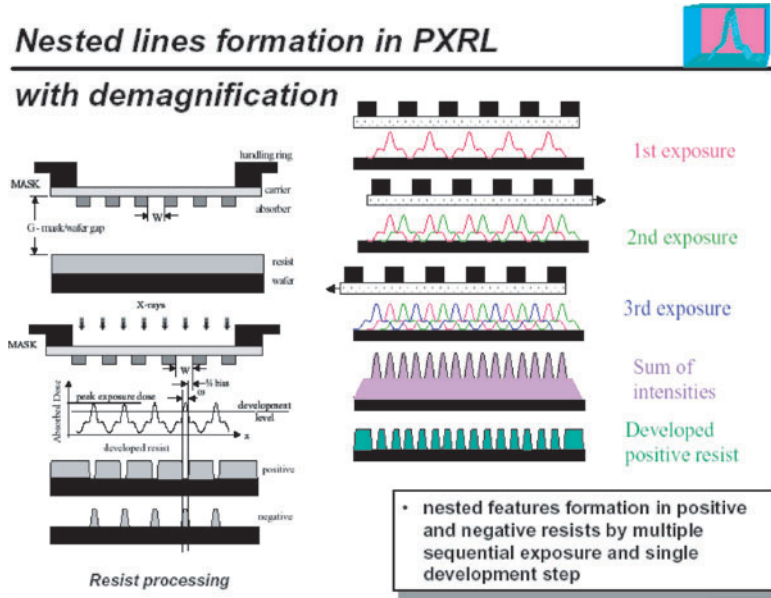
Figure 2. Schematic diagram shows dense lines that can be developed from multiple exposures of an individual clear mask feature demagnified by bias.

background. The ratio of pitch to line-width is reduced to 2 : 1, i.e. half pitch, by the method of multiple exposures with single development. The process is rapid because the stepping is typically blind and peaks are intense.

3. Experimental demonstrations

The following demonstrations were performed on a modified Suss XRS-200/2M x-ray stepper, owned by the Center for Nanotechnology and located on beamline ES-4 on the Alladin storage ring at the University of Wisconsin-Madison Synchrotron Radiation Center. A combination of optimized lithographic process and exposure conditions allowed the formation of lines down to 25 nm at 15–30 μm gaps for both negative (SAL605) and positive (UV-3, APEX-E) resists [1]. The stepper was upgraded for 130 nm alignment. The modern, commercially available equivalent is capable of 45 nm alignment.

3.1. Line prints using demagnification by bias

To demonstrate the fact of demagnification by bias, various line prints have been recorded using a synchrotron radiation source with a typical broadband radiation dose centred about 0.8 nm wavelength [2–5]. Some examples are shown in figure 3. A SAL 605 resist was used to form the figures 3(*a*) and (*b*) and PMMA was used for figure 3(*c*). Figure 3(*b*) shows evidence of mechanical failure in the resist due to the high aspect ratio (43 nm wide, 250 nm high) in the printed lines, which have folded over in parts. The failure is readily circumvented by either reduced resist thickness or by implementation of more robust resists.

The masks used in these experiments were conventional gold absorber on silicon nitride film substrates patterned by an electron beam. The gold is typically 350 nm thick [2]. These masks are suitable for development applications,

though amorphous silicon nitride is known to be less robust than crystalline silicon carbide substrates used with tantalum compounds as absorbers [8].

3.2. Nested features

Figure 4(*a*) is a simulation of low pitch 45 nm lines for printing after double exposure. This simulation corresponds to the print in figure 4(*b*) and follows the schematic diagram in figure 2, except that the latter is for triple exposures closer to the CC (see later and [2]). The height fluctuations in the unexposed regions of the positive resist are thought to be due to a proximity effect in the resist development and are not significant.

4. Temporal and spatial incoherence

4.1. The CC in one dimension

Consider firstly the CC [2] as it applies in the imaging and printing of one-dimensional features such as parallel lines. Figure 5 shows a schematic exposure system. Parallel rays of radiation pass through a clear mask feature and form a Fresnel pattern, or demagnified image, at a distance G below the mask feature. One ray is axial. A second ray suffers a phase lag that depends on the distance, s, from the centre line of the clear mask feature; i.e. the phase lag suffered by this ray at the resist depends on $2\pi s^2/\lambda$, when the wavelength is λ. The amplitude at the wafer depends on the vectorial sum of the amplitudes of all rays passing through the clear mask feature.

Consider the dimensionless spatial coordinate, v, defined as

$$v = s\sqrt{\frac{2}{G\lambda}} = \sqrt{2N_{\mathrm{F}}}, \tag{1}$$

where s is a distance measured from the axis of the clear mask feature/clear mask feature in its plane (figure 5); G is the width of the mask–wafer gap; λ is the wavelength of the radiation

(a)

180 nm

61 nm

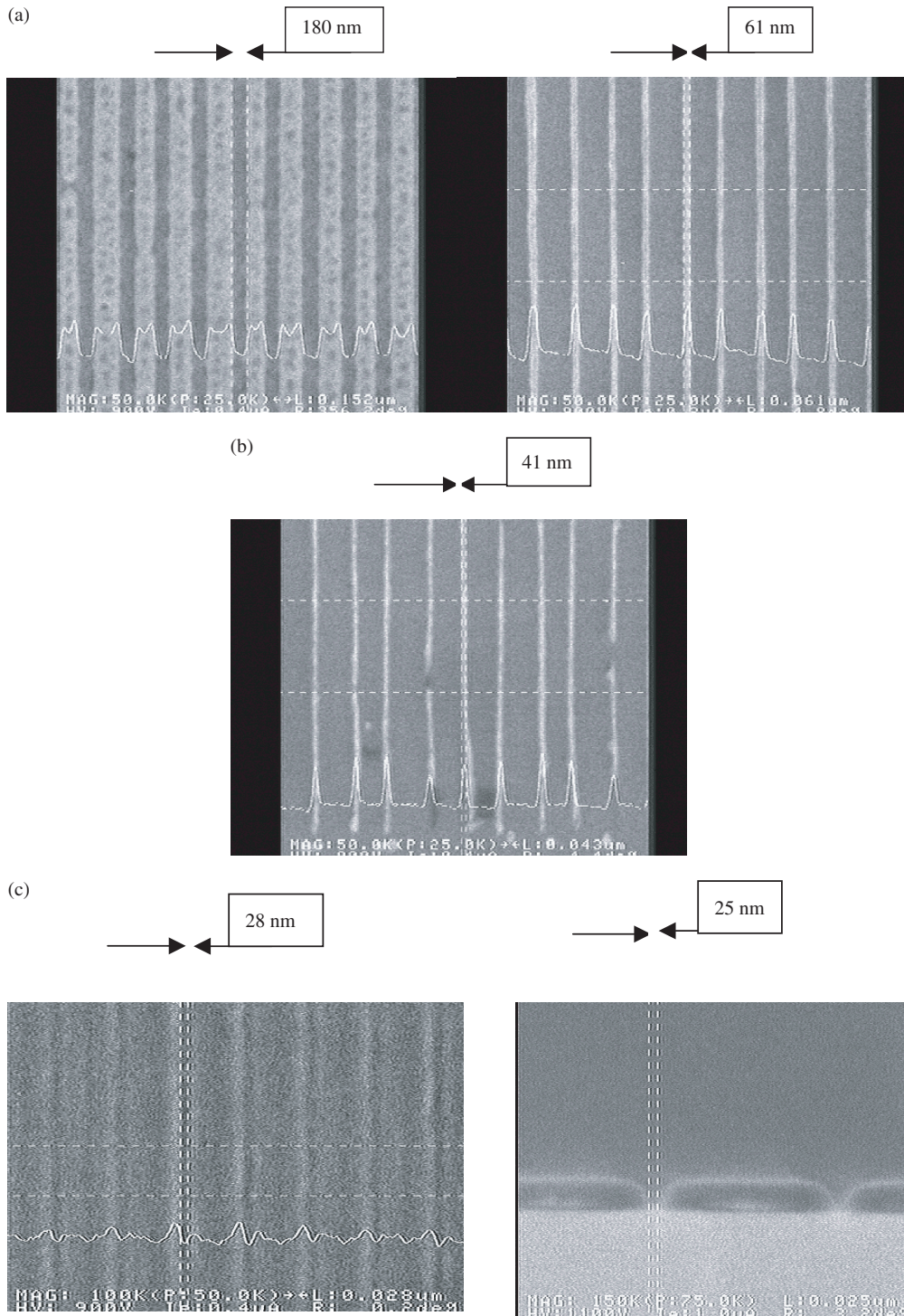
(b)

41 nm

(c)

28 nm

25 nm

Figure 3. (*a*) 61 nm lines printed in SAL 605 negative resist (right) using a mask (left) with 152 nm lines and 360 nm period. (*b*) 43 nm lines printed in SAL605 negative resist using 152 nm lines on a mask. Mechanical failure in the resist is due to a high aspect ratio. (*c*) 28 nm print (left) and 25 nm print (right) in PMMA.

used, and N_F is the number of Fresnel half zones across the clear mask feature.

If Δs is the clear mask feature width and Δv is the dimensionless spatial coordinate corresponding to Δs at a given G and λ, then

$$\Delta v = \Delta s \sqrt{\frac{2}{G\lambda}}. \qquad (2)$$

Δv can be called the dimensionless slit width. The vectorial addition of the amplitudes and phases of rays passing through the clear mask feature, and interfering constructively at the plane of the wafer, can be summed over all transmitted rays. The amplitudes are represented mathematically with well-known Fresnel integrals or can be summed graphically with Cornu's spiral [19], i.e. the vibration curve (shown in figure 6(*a*) when $\delta v = 0$). The amplitude of the Fresnel
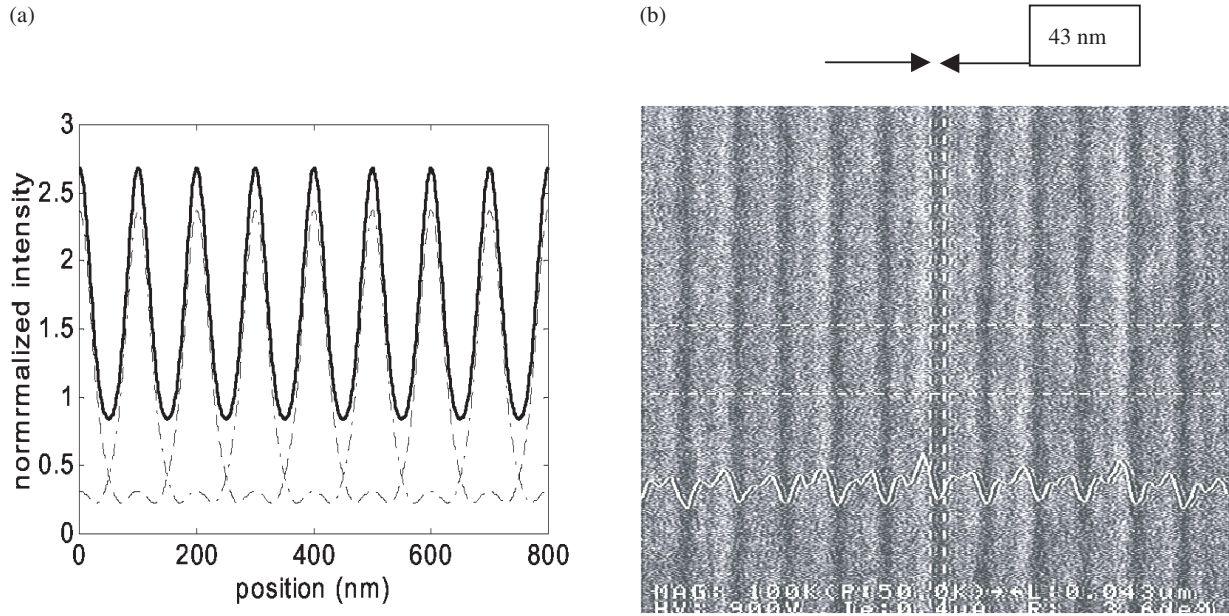
(a)

(b)

43 nm

Figure 4. (*a*) Simulation of intensity deposited by double exposure. (*b*) 43 nm lines with 155 nm pitch obtained by a double exposure–single development technique from a mask pattern with 310 nm period and 160 nm features.
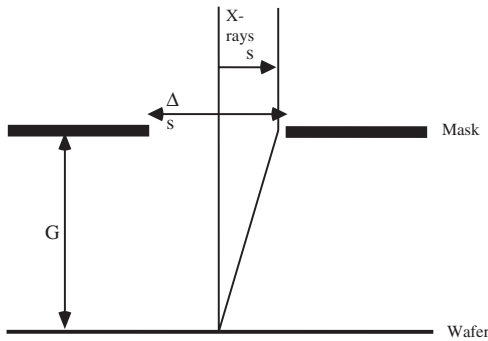

Figure 5. Rays that are transmitted off-axis suffer phase shifts equal to $2\pi s^2/\lambda$. These shifts are represented on the Cornu spiral in figure 6, where s is converted to the dimensionless spatial coordinate, ν, as described in the text.

pattern at a point on the wafer can be found by summing amplitudes and phases of corresponding rays [19]. The vectorial summation is found graphically by connecting two points on Cornu's spiral. Summing over rays for which $\Delta s/2 \geqslant s \geqslant -\Delta s/2$ (or $1.2 \geqslant \nu \geqslant -1.2$) at the CC, their amplitude, at the wafer on-axis, is the longest vector that joins the extremities of the Cornu spiral (vector C in figure 6(*a*)). The square on this vector is the maximum intensity at the highest peak shown in figure 6(*b*). Off-axis at the wafer, asymmetric vectors on the spiral are used to represent, in the conventional way, vectorial sums of ray amplitudes [19].

The CC [2] occurs when the width of a transmitting mask feature, Δs, is related to the mask–wafer gap, G, and the x-ray wavelength, λ, by the equation:

$$\frac{\Delta s}{\sqrt{\lambda G}} = 1.7 \qquad (3)$$

i.e. $\Delta \nu = 6^{1/2} \sim 2.4$.

The CC has a clear theoretical meaning with practical implications. However, there is wide latitude in setting the conditions—through the selection of wavelength, mask feature size and gap—that are not practically critical. Cornu's spiral applies to the imaging of a long slit with monochromatic radiation; but we extend it, as in the example later, to applications using broadband illumination having temporal incoherence, with masks supplying additional spatial incoherence.

Notice meanwhile that, by holding the dimensionless $\Delta \nu$ in equation (2) constant, the gap, G, changes with the square of the slit width, Δs, and that G depends inversely on λ. This is an important reason for demagnifying and a new reason for using shorter wavelengths [15].

4.2. The CC with broadband illumination

Secondly, with broadband illumination, simulations require independent vectorial addition for both temporal and spatial coherence. It follows from equation (1) that $\delta \nu/\nu = -\delta \lambda/2\lambda$. In figure 6(*a*), the Cornu's spiral for monochromatic radiation, $\delta \lambda = 0$, is averaged and represented on modified spirals. Vectorial additions of rays, to account for the temporal coherence, was made for $\delta \nu/\nu = 0, \pm 0.2, \pm 0.4$ and ± 0.6 as shown in the figure. The spirals converge faster with increasing bandwidth. A typical experimental configuration uses $\delta \nu/\nu \sim 0.2$. Subsequently summing for rays across the dimensionless slit width provides corresponding aerial profiles in the conventional way [19]. This second summation is for spatial coherence. Examples of corresponding profiles, at CC, are shown in figure 6(*b*).

The new significance of these plots lies in the inflection points where the graphs at various $\delta \nu$ cross over. The inflection points closest to the axis ($\nu = 0$) occur at $\nu = \pm 0.36$, where the slope is steeper, and at $\nu = \pm 0.88$, where the slope is shallower. A steep slope is valuable for CD control in printing. It is interesting, furthermore, that the inflection points occur on the same ordinate scale as the incident dose (level 2) at the clear mask feature.
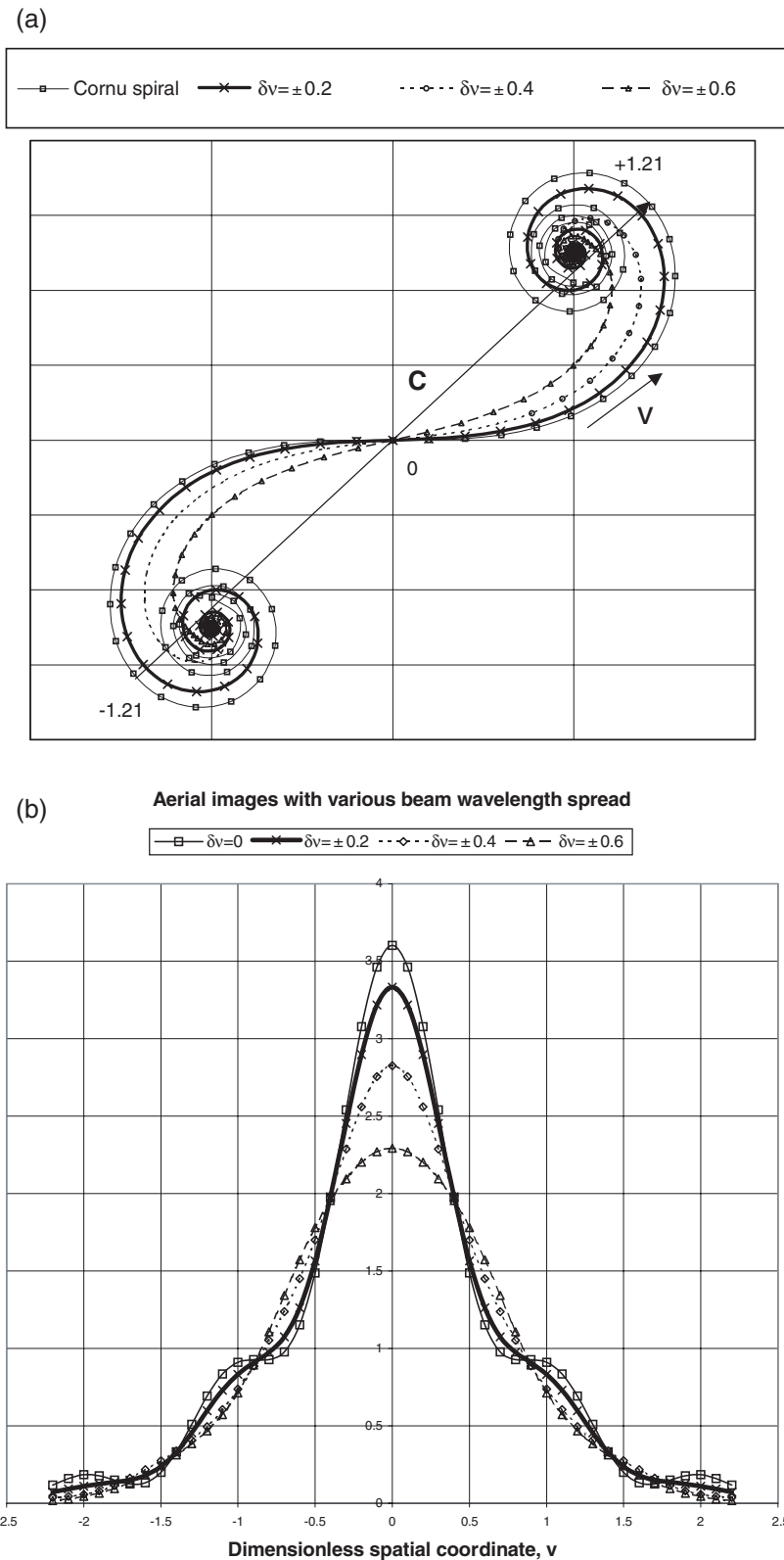
2475

(a)

(b)

Aerial images with various beam wavelength spread

Dimensionless spatial coordinate, v

Figure 6. (*a*) Cornu's spiral (see legend) representing relative phases of rays transmitted by a slit onto a wafer. The vector C represents the sum of phases of transmitted rays striking the wafer, at the critical condition, on the slit axis at the wafer. To account for broadband illumination, other spirals are formed by averaging over dimensionless spatial coordinates: typically, when $\delta v = \pm 0.2$, and also when $\delta v = +0.4$ and $\delta v = +0.6$. These spirals demonstrate the effects of temporal incoherence. (*b*) Aerial images at the CC corresponding to monochromatic x-rays, $\delta v \sim 0$ (see legend), typical broadband, $\delta v = +0.2$, and also $\delta v = +0.4$ and $\delta v = +0.6$. Not the inflection points at $v = 0.36$, where the slope is steepest, and at $v = 0.88$, where the slope is shallowest. At the CC, for which $\Delta v = 2.4$, the slit edges lie geometrically opposite the dimensionless points $v = +1.2$ and -1.2 on the wafer. (Courtesy: SPIE Optical Society of America, vol 5037 [1].)

When $\nu = 0.88$ and $\delta\nu = 0$, the printing definition is extremely poor. This is close to the case used in traditional $1\times$ proximity printing [9], where $\nu = 1.2 = \Delta\nu/2$ at the CC. Contrast is then further degraded with broadband as can be seen in figure 6(b) and additionally degraded by sidebands, i.e. compared with the aerial image shown in this figure. Sidebands at $\nu > \Delta\nu/2$ are increased by residual transmission from the mask absorber [2] and are further increased in masks containing periodic structures. The fuzzy contrast, sometimes difficult to predict, that was traditionally used in $1\times$ PXL is completely avoided in near field, where rapid exposures are made, high on the aerial image instead of at the base.

However, the inflection points demonstrate a further optimization of demagnification in near field. Previously, we have proposed [2–5, 14] that 'demagnification by bias' is selectable, depending on chosen development level and that optimization depends on various factors including fabricability of masks and multiple exposure systems. It now appears that an additional feature needs to be taken into account and this may often dominate: where CD control is critical, contrast is highest at the inflection point, i.e. at a demagnification of $3\times$ or $1/0.36$.

4.3. The CC for two-dimensional features

Consider thirdly the CC for two-dimensional, asymmetric clear mask features. Since the CC depends on clear mask feature size, Δs, it cannot be maintained for two different dimensions at one time. CC then refers, by our convention [2, 14], to the smaller dimension where print resolution is more critical.

Consider in consequence, features produced in the less-critical, longitudinal direction of a rectangular mask. To understand the independent effects of mask feature shape, wavelength and gap for two-dimensional images, idealized simulations were performed for the intensities below the mask. A multislice method written in the SEMPER [20] image processing program was used. The program allows the Fresnel diffraction from arbitrarily shaped masks in one or two dimensions to be calculated at any distance from the mask. Examples of imaging with monochromatic radiation and with broadband illumination, both at CC and away from CC, have been previously described [14, 2]. With monochromatic radiation, artefacts in the two-dimensional pattern occur. These were previously characterized [2] as 'ripple' and 'bright spots' and both are reduced in effect when a broad beam is used. The levelling is a consequence of temporal incoherence and corresponds to spiral constriction with increasing bandwidth, $\delta\nu$ (as shown in figure 6(a)).

To reduce the undesirable effects of ripple and bright spots further, the spatial incoherence in the aerial pattern was increased by an inverted variant of optical proximity correction [14, 2]. In particular, it was found that a blurred $45°$ indent, at the ends of a rectangular pattern, results in a reduction of ripple and bright spots to insignificance when a broad beam is additionally used, typically, as before. Residual ripple and bright spots can be seen in figure 7.

Near field can be used equally to print patterns of arbitrary shape, though optimization occurs through a correct use of temporal and spatial incoherence. As an example, figure 7 shows a flag shaped pattern and the corresponding aerial image when the gap is set critical ($\Delta\nu = 2.4$) for the narrow part of the flag pole. Blurred indents are employed at the ends of the pole, and the corners of the flag are also blurred. The pole can be conveniently printed $3\times$. Notice that the width of the flag then has $\Delta\nu \gg 2.4$, and it is printed with a smaller proportionate bias, close to $1\times$. The effects of various indents are shown in the figure. The mask showing the best print profile is the fourth down. For this mask, profiles of the simulated intensities (a) vertically along the flagpole centre and (b) horizontally across the flag centre are shown in adjacent boxes in the figure. The results show how, by employing temporal and spatial incoherence, any shape can be printed with high resolution using near field x-rays. Notice that in printing complex shapes the requirement for half pitch is relaxed.

Figure 8(a) shows a simulated image of a bridge corresponding to the mask in the upper figure. If the bridge is 100 nm wide in the mask a print, 30 nm wide will be readily obtained using wavelengths $1.2 > \lambda > 0.6$ nm. An unfortunate horizontal ripple occurs at the bridge contact. The ripple can, in principle, be reduced by wavy edges on the mask as shown in figure 8(b); but with an introduction of artefacts. Various simulations have been performed and a typical result is shown in figure 8(b) as an illustration. The simulations were again made with the SEMPER program. A combination of ten x-ray wavelengths with $0.62 \leqslant \lambda \leqslant 1.24$ nm was used to simulate a synchrotron spectrum for a mask–wafer gap of 4.3 μm, as is critical for a 100 nm wide bridge at the mask. In the figure, waves are applied to the mask edge at the horizontal contacts. The waves shown are square or saw tooth, using an amplitude of 40 nm. Figure 8(b) further illustrates the effects of two-dimensional Fresnel diffraction. In selected conditions, isolated islands can be imaged with high contrast at demagnification about $6\times$. The examples illustrate ways in which two-dimensional Fresnel diffraction could be used to produce fine, enhanced images. These results indicate moreover that alternative ways are needed to eliminate ripple troughs at the contacts, including, possibly, phase shifted edges, or more simply, double exposures with a vertical shift of the pattern. It is less important to reduce peak maxima than to increase trough minima since these become critical for uniform development at a selected level.

If the pattern in figure 8(a) is shifted between double exposures, the principal peak and trough on the horizontal contact ripple can be smeared. In figure 8(c), simulated profiles of the contact edge ripple from figure 8(a) are shown for the monochromatic case for a single exposure and for a series of translations along the dimensionless coordinate. The profiles are calculated in the normal way for Fresnel diffraction from a knife edge [19] using the Cornu spiral in figure 6(a). With the configuration previously used in figure 8(a), a translation of 29 nm corresponds to a dimensionless translation $D\nu = 0.7$ and superposes peak on trough. More precisely, this superposition occurs when the dimensionless translation is $D\nu = (\frac{7}{2})^{1/2} - (\frac{3}{2})^{1/2}$. Notice that, in this monochromatic case, the first peak and trough are more thoroughly smeared than the second trough. Considering next the more realistic case of polychromatic radiation of typical spread, $\delta\nu = 0.2$,
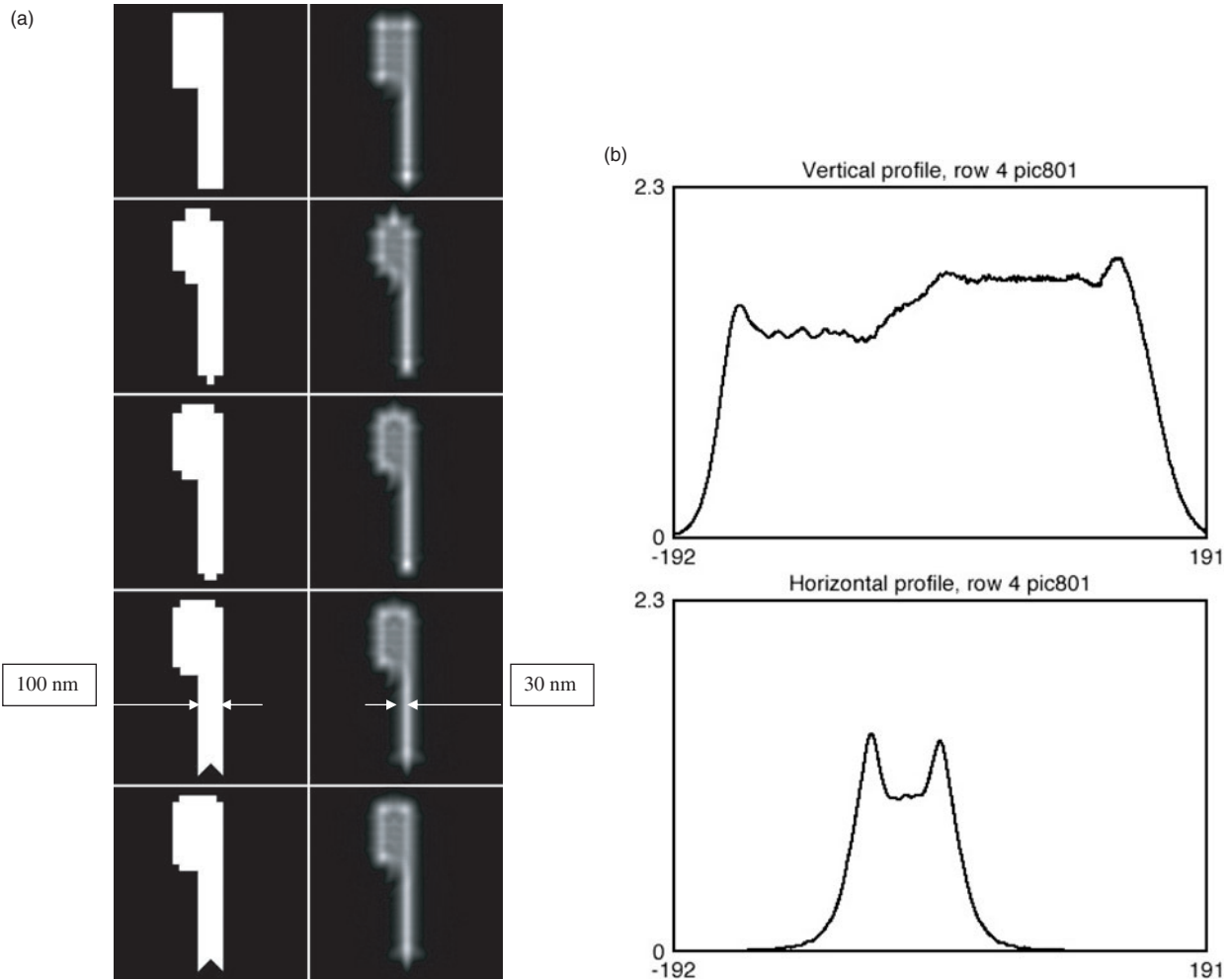
(a)

100 nm

30 nm

(b)

Vertical profile, row 4 pic801

2.3

0

-192   191

Horizontal profile, row 4 pic801

2.3

0

-192   191

Figure 7. (*a*) Flag pole patterns (left) with pole $150 \times 600\,nm^2$ plus flag $450 \times 300\,nm^2$ and corresponding simulated images (right) at the CC using broadband wavelengths, $0.62 < \lambda < 1.24\,nm$. Spatial incoherence and the resulting uniformity of exposure are increased by the use of the various indents shown. (*b*) Profiles of the simulated image on the fourth row both vertically down the flag pole centre and horizontally across the flag centre. A development level can be chosen to print the pole $3\times$, with the broader flag close to $1\times$.

and using the appropriate modified spiral from figure 6(*a*), the resulting profiles in figure 8(*d*) show that the second trough is also smeared. The translation that reduces ripple most occurs around $Dv = 0.5$, corresponding to a translation of 21 nm. Simulations can obfuscate if employed without care; but these profiles provide clarity in understanding. The vertical translations between double exposures do not in any way sacrifice the printable resolution of the bridge itself; an optimal translation serves solely to control the horizontal ripple troughs at the contacts.

The method of double exposures, used here to reduce ripple at the contacts, provides a further degree of freedom in further reducing the ripple in two-dimensional structures such as the flag in figure 7(*a*).

4.4. Other effects of coherence

A further consequence of the diffraction is a reduction in printing errors due to mask defects when compared with $1\times$ PXL. Inhomogeneities in mask patterns are smoothed by Fresnel diffraction at the print surface. Examples of

such reductions are discernible in figure 3(*a*) and elsewhere [2, 3].

4.5. Extensibility to 15 nm and further

Various facts lead us to revise our previous estimates [2] of the extensibility of near field methods. Recent studies that include treatments of blur [17, 18] when combined with a careful study of present results, especially the 25 nm print in figure 3, together with equivalent earlier, but overlooked, reports [21, 22] lead to a conclusion that previous estimates of photoelectric blur were exaggerated. It was previously supposed that the smallest feature size that can be printed by PXL results from the minimum due to competing effects of diffraction and photoelectric blur and that these are both dependent on the energy of photons used. The experimental results cited would have been impossible if those previous estimates of blur are valid. In particular, the blur in PMMA produces negligible broadening at 20 nm print resolution when used with 0.8 nm x-rays incident on the mask and the printed feature size is dominated by diffraction [1]. This is especially
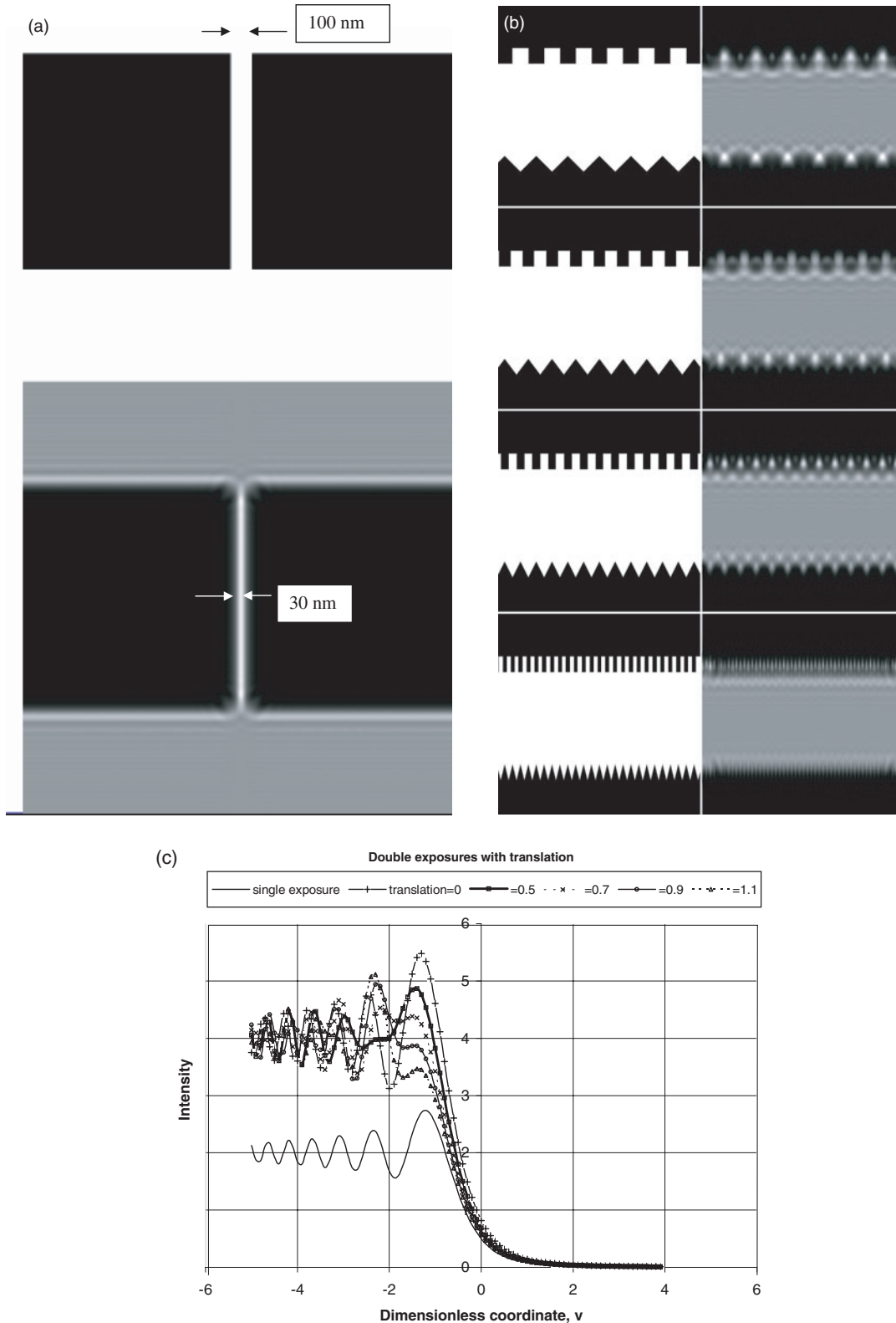
Figure 8. (*a*) Mask for bridge (top) 100 nm wide and image simulation made using SEMPER as before with wavelength $0.6 < \lambda < 1.2$ nm, but with mask–wafer gap $G = 11.2\,\mu$m. A typical print will be $3\times$ for 30 nm at the bridge and just less than $1\times$ at the contacts. (*b*) Illustration of reduction in ripple due to square waves and triangular waves as shown and with wavelengths from top to bottom of 160, 120, 80 and 40 nm and with 40 nm amplitude in all cases. (*c*) Simulated profiles showing reduction in ripple due to double exposure of mask in figure 10(*a*) using monochromatic radiation. The figure shows the profile of a single exposure knife edge after Fresnel diffraction for comparison. Also shown are profiles due to double exposures with translations corresponding to $\nu = 0$, 0.5, 0.7, 0.9 and 1.1. A vertical shift of dimensionless coordinate $\nu = 0.7$ corresponds to a translation of 29 nm between exposures. (*d*) Simulated profiles for typical polychromatic double exposure where $D\nu = 0$, 0.3, 0.5, 0.7, 0.9 and 1.1. The energy spread is $\delta\nu = 0.2$ (see figure 6(*a*)). The best condition is found around $D\nu \sim 0.5$ when horizontal ripple at the contacts is controlled.
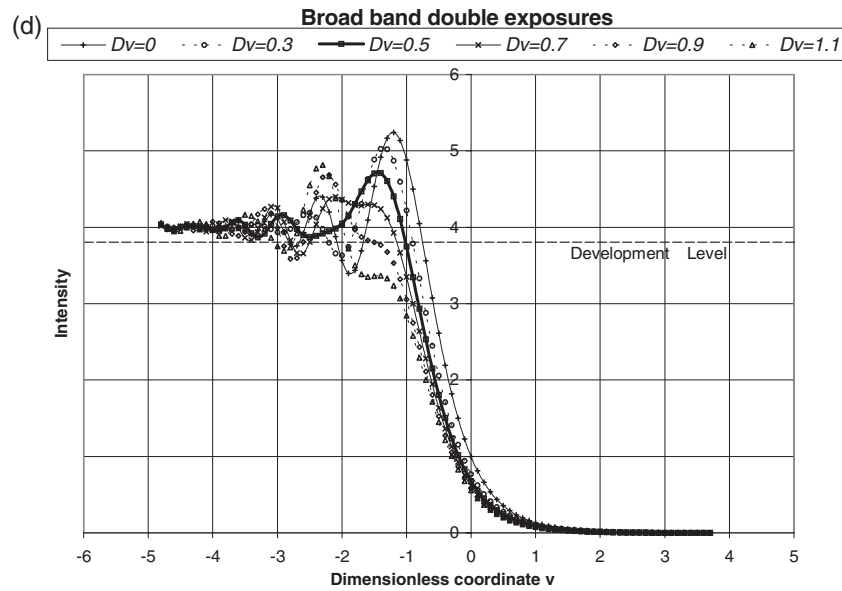
2479

Figure 8. (Continued.)

Table 1. Comparison of power, thoughput and divergence of various sources.

	Emission (W sr)	Capture angle (msr)	Exposed area (mm)	Intensity delivered (mW cm^{-2})	Exposure time (s)[a]	Throughput compared (8″wph)	Local divergence (mrad)	Penumbral blur (nm)	Global divergence (mrad)	Run-out (max) (nm)
Helios II with collimation	60 000 ~orbit plane	0.015	50 × 30 scanned	100	0.6	120[b]	0.1	1	1.5 vertical 2.5 horizontal	15 25
	60 000	0.015	50 × 30	100	0.6	120[b]	~0.1	~1	<0.25[c]	2[c]
Laser with collimator	3.8 3.8	0.9 35	50 × 50 22 × 22	~0.2 ~0.8	300 75	1 1.4	0.1 4	1 40	25 <0.5	250 <5
Squeezed plasma	~4	0.9	50 × 50	~0.2	300	1	1	10	25	250

[a] Assuming chemically amplified resist with dose sensitivity 60 mJ cm^{-2}.

[b] Allowing 0.4 s alignment.

[c] Mask magnification error also correctable.

the case when demagnification by bias is deliberately used as in near field. Though primary photoelectric blurring is broad, the printed contrast, in fact, depends on the Auger electrons, and their range is not only considerably smaller than that of the primaries, but does not change with increasing incident photon energy. This range only changes significantly with resist composition, which can be selected for optimization.

Blurring due to the range of Auger electrons is small down to configurations designed for 15 nm prints with near field. The diffraction limits depend on the experimental k value (k = smallest print feature size/$(\lambda G)^{1/2} \sim 0.15$) demonstrated using demagnification by bias on isolated lines [1]. At dimensions for 15 nm prints, the gap approaches an experimental limit of about 5 μm, and the printing is facilitated if a restriction to half pitch is relaxed. Since PMMA has lower etch resistance and is less sensitive than chemically amplified resists such as SAL605, optimization will benefit from a selection of new resists beyond those currently used in both PXL and 248 nm optical lithography. Some of the requirements in resist development are common to all next generation lithographies and mutual transference is anticipated

for extension to 15 nm prints. For print features down to 35 nm, normal ultraviolet (UV) resists are sufficient and readily available.

4.6. Blur and run-out in PXL

Consider next, features in PXL that vary with the different sources that are sometimes used: the synchrotron source; the laser plasma point source that can be used without collimation [23] or with collimation [24, 25]; and the pinched plasma source employing an electric discharge [26].

All these sources use a broadband spectrum of wavelengths up to 50% of mean wavelength and share this advantage over projection methods that are in comparison complex, slow and costly. The synchrotron is especially intense because of the collimation provided by relativistic flattening of space onto the orbit plane and this is reflected in table 1. The table also shows comparatively, the specific source properties of local and global divergence. These properties determine blur and 'run-out' (figure 9(*a*) and table 1).

On a synchrotron, penumbral blur depends on its effective source size, *z*, namely the electron beam cross-section as
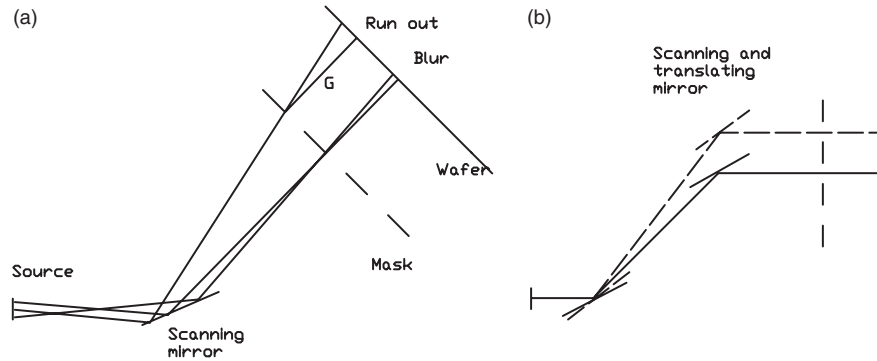
Figure 9. (*a*) Schematic diagram showing the occurrence of blur and of run-out or 'magnification error'. (*b*) Schematic diagram showing magnification correction by a scanning and translating mirror with x-ray beam incident horizontally on the mask. Not shown, for simplicity, is the conventional horizontally collimating mirror close to the tangent point, which can be controlled to produce magnification corrections in the horizontal plane.

projected by the orbital motion. The projection makes negligible difference, and a typical blur, B, in lithography systems having beam line length, x, from tangent point to mask, is given by $B = zG/x \sim 1\,\text{nm}$[4]. The 'run-out', δM, or 'magnification error', depends on the mask width, w, and gap $\delta M = wG/2x$.

If not corrected, run-out causes a magnification error in $1\times$ PXL. Happily, several methods are available for correction. In one of these, a mirror is inserted between the first scanning mirror and the mask (figure 9(*b*)). The mirror is controlled to scan and translate in accord with the first scanning mirror [27], run-out is virtually eliminated in the vertical plane. Likewise, the run-out can be corrected in the horizontal plane by the horizontally collimating mirror normally placed close to the synchrotron tangent point in order to optimize collection. By an extension of the technique [28] with various controls, magnification corrections for the mask or wafer can also be made both horizontally and vertically. These optical methods are in addition to several other methods that have been proposed: the mask can be strained mechanically in vertical and horizontal planes [29] or dynamic scanning of mask and wafer can produce vertical corrections [30]. On the synchrotron, blur and run-out are most readily controlled and adapted to overlay requirements in multiple level printing of integrated circuits.

5. Conclusions

Extension of PXL to about 15 nm print feature sizes can be obtained by using the near field. In doing so, the mask–wafer gap, which scales with the square of the (critical) clear mask feature size, increases with respect to traditional $1\times$ PXL. Spatial and temporal incoherence are invoked to identify demagnification regimes that provide enhanced CD control. 'Demagnification by bias', about $3\times$ for critical features, allows optimum discrimination in printing edge features. This is due to an inflexion point in Fresnel diffraction when the wafer is placed at the CC. By contrast, the analysis shows that exposures with traditional $1\times$ edges often lie close to plateaux—especially when broadband illumination is

used—where intensity discrimination, employed critically in the printing, is minimal. A new method of double exposures is applied to reduce ripple in two-dimensional prints. Moreover, near field x-ray lithography has further important advantages in both the control of printing and in increased wafer throughput, plus increased mask feature size and gap width, in addition to the outstanding feature of extensibility beyond 20 nm. The method opens the way to the manufacture of micromachines and integrated circuits of such small dimensions, whether using modern compact synchrotron light sources or, at a slower rate, with laboratory sources.

Acknowledgments

References

[1] Bourdillon A J, Williams G P, Boothroyd C B and Vladimirsky Y 2003 *Proc. SPIE Microlithography* vol 5037, pp 622–3
[2] Bourdillon A J, Boothroyd C B, Kong J R and Vladimirsky Y 2000 *J. Phys. D: Appl. Phys.* **33** 1–9
[3] Vladimirsky Y, Bourdillon A J, Vladimirsky O, Jiang W and Leonard Q 1999 *J. Phys. D: Appl. Phys.* **32** L114–18
[4] Kong J R, Vladimirsky Y and Quinn L 2000 *Proc. MNE 2000 (Jena, Germany, 18–21 September)*
[5] Kong J R, Quinn L, Vladimirsky Y and Bourdillon A 2000 *Proc. SPIE Microlithography 2000 (Santa Clara, 27 February–3 March)*
[6] Vladimirsky Y and Bourdillon A J 2002 *US Patent No* 6383698
[7] *Solid State Technology* February 2000, News Item **43** pp 18–23
[8] *Proc. Intrnational SEMATECH Workshop (Colorado Springs, 7–10 December 1998)*
[9] Neureuther A R 1980 Microlithography with soft x-rays *Synchrotron Radiation Research* ed H Winich and S Doniach (New York: Plenum)
[10] Vladimirsky Y 1998 Lithography *Vacuum Ultraviolet Spectroscopy II* chapter 10, pp 205–23 J A Samson and D L Ederer (ed) *Experimental Methods in the Physical Sciences* vol 32 (New York: Academic)
[11] Cerrina F 1997 'X-ray lithography' *Handbook of Microlithography, Micromachining, and Microfabrication* vol 1, ed P Rai-Choudhury (Bellingham: SPIE Press) chapter 3, pp 253–319

---

[4] That is less than the estimate of 5 nm estimated in [12]

[12] Krasnoperova A A, Rippstein R, Flamholz A, Kratchmer E, Wind S, Brooks C and Lercel M 1999 *Proc. SPIE Conf.* vol 3676, pp 24–39

[13] Vladimirsky Y 1999 Introduction: limits or limitations *Proc. SPIE Conf.* vol 3676, pp xvi–xvii

[14] Bourdillon A J and Boothroyd C B 2001 *J. Phys. D: Appl. Phys.* **34** 3209–13

[15] Yang L and Taylor J W 2001 *J. Vac. Sci. Technol.* B **19** 129–35

[16] Khan M, Han G, Bollepalli S B, Cerrina F and Maldonado J 2000 *J. Vac. Sci. Technol.* B **17** 3426–32

[17] Khan M, Han G, Tsvid G, Kitayama T, Maldonando J and Cerrina F 2002 *J. Vac. Sci. Technol.* B **19** 2423–7

[18] Vladimirsky O, Dandekar N, Jiang W, Leonard Q, Simon K, Bollepalli S, Vladimirsky Y and Taylor J W 1999 *Proc. SPIE Conf.* vol 376, p 92

[19] Jenkins F A and White H E 1976 *Fundamentals of Optics* 4th edn (New York: McGraw-Hill)

[20] Saxton W O, Pitt T J and Horner M 1979 *Ultramicroscopy* **4** 343

[21] Early K, Schattenburg M L and Smith H I 1990 *Microelectron. Eng.* **11** 317–21

[22] Chen *et al* 1998 *J. Vac. Sci. Technol.* B **16** 3521–5

[23] Gaeta J *et al* 2002 *Japan J. Appl. Phys.* **41** 4111–21

[24] Forber R A, Chen Z W, Menon R, Grygier R, Mrowka S, Turcu I C E, Gaeta C J, Cassidy K and Smith H I 2002 *J. Vac. Sci. Technol.* B **20** 2984–90

[25] Turcu I C E *et al* 2003 *Proc. SPIE Microlithography* vol 5037 (23–27 February) at press

[26] Vladimirsky Y 2003 Course notes *SPIE Short Course on X-ray Lithography*

[27] Fuji K 1989 *US Patent No* 4803713

[28] Mitsui S and Murooka K 2000 *US Patent No* 6078641

[29] Chen A C 1995 *US Patent No* 5504793

[30] Hasegawa T and Miyachi T 2000 *US Patent No* 6078640